PCCP

PAPER

View Article Online
View Journal | View Issue

Cite this: *Phys. Chem. Chem. Phys.*, 2025, **27**, 14000

Biomass-derived macroporous carbon–tin oxide composites as stable and high-capacity anodes for lithium-ion and sodium-ion batteries: experimental study and GFN1-xTB calculations†

Glaydson Simoes dos Reis,*[a] Chandrasekar M Subramaniyam,[b] Alejandro Grimm,[c] Mahiar Max Hamedi,[d] Palanivel Molaiyan,[e] Flaviano García-Alvarado,[b] Ulla Lassi,[e] Jakub Goclon[f] and Shaikshavali Petnikota[c]

To produce high-performance anode materials for lithium/sodium batteries *via* sustainable strategies is still one of the most essential tasks in battery research. A biomass-based carbon–tin oxide composite (BC/SnO_2) is prepared through pyrolysis of birch tree waste using phosphoric acid as an activator and its electrochemical performance as a sustainable anode material in lithium-ion batteries (LIBs) and sodium-ion batteries (NIBs) is tested. The physicochemical characterization results proved that SnO_2 has a remarkable impact on BC/SnO_2 porosity, morphology, and physicochemical features. Due to these favorable properties, the BC/SnO_2 anode exhibited far better performance for LIBs and NIBs than bare carbon (BC). Against Li metal, the BC/SnO_2 anode delivered a specific capacity of 319 mA h g^{-1} while BC delivered only 93.2 mA h g^{-1} (at 1C) at the end of 120 cycles. The BC/SnO_2 composite showed excellent rate performances at different current densities, exhibiting a capacity of 453 mA h g^{-1} at the end of 120 cycles. Upon testing against sodium metal, the BC/SnO_2 composite exhibited better cycling stability than BC (233 mA h g^{-1} compared with 165 mA h g^{-1}) at 100 mA g^{-1} for 120 cycles. A theoretical investigation of the interactions between BC and SnO_2 was performed using the semi-empirical GFN1-xTB method. The stability of the mixed system at high temperatures was confirmed using molecular dynamic simulations. Finally, we analyzed the electronic properties of the BC/SnO_2 composite and drew conclusions about the electrical conductivity. Therefore, our research strategy helps to produce sustainable high-specific capacity anode materials from biomass resources for building cost-effective metal-ion batteries.

Received 18th March 2025,
Accepted 4th June 2025

DOI: 10.1039/d5cp01053e

rsc.li/pccp

1 Introduction

Over recent years, problems related to both environmental issues and the depletion of fossil energy have pushed society toward the development of more sustainable, renewable, and cleaner energy materials and devices. Furthermore, the sharp increase in the production of electric energy from renewable resources (solar, wind, tidal, *etc.*) is not only a consequence of the awareness of the climate impact of the use of fossil fuels but is also economically beneficial.[1] However, solar and wind energy are characterized by non-continuous production and, therefore, require powerful energy storage systems to store and distribute electricity according to consumers' needs.[1] Lithium-ion batteries (LIBs) are widely employed and are the dominant technology for small to large energy storage (ES) applications, such as portable electronics, electric vehicles, and grid applications.[2,3] However, due to the use of critical elements (lithium, graphite) and/or their low availability, the high demand for ES cannot rely only on LIBs. Furthermore, graphite is the most

[a] *Laboratory of Industrial Chemistry and Reaction Engineering, Faculty of Science and Engineering, Åbo Akademi University, 20500, Åbo/Turku, Finland. E-mail: glaydson.simoesdosreis@abo.fi*
[b] *Chemistry and Biochemistry Dpto., Facultad de Farmacia, Universidad San Pablo-CEU, CEU Universities, Urbanizacion Montepríncipe, 28668Boadilla del Monte, Madrid, Spain*
[c] *Department of Forest Biomaterials and Technology, Biomass Technology Centre, Swedish University of Agricultural Sciences, Umeå, SE-901 83, Sweden*
[d] *Department of Fibre and Polymer Technology, School of Engineering Sciences in Chemistry, Biotechnology and Health, KTH Royal Institute of Technology, Teknikringen 56-58, SE-100 44, Stockholm, Sweden*
[e] *Research Unit of Sustainable Chemistry, University of Oulu, P.O. Box 3000, FI-90014, Oulu, Finland*
[f] *Faculty of Chemistry, University of Bialystok, Ciolkowskiego 1K, 15-245, Bialystok, Poland*

† Electronic supplementary information (ESI) available. See DOI: https://doi.org/10.1039/d5cp01053e

used anode material in LIBs, however, it cannot meet the increasing demand for high-performance ES devices due to its low theoretical capacity (372 mA h g^{-1}).[4,5]

These issues ignited a tireless pursuit of more sustainable, greener, and cheaper battery systems such as sodium-ion batteries (NIBs).[6–8] NIBs are set to be the next-generation commercial batteries with the potential to replace LIBs due to their more sustainable approach, enormous and abundant sodium resources, and low-cost and competitive electrochemical performances.[8] Besides, the dominant anode material for NIBs is hard carbon, which can be easily synthesized from sustainable resources such as biomass precursors.[9] Hard carbons are composed of disordered graphene-like structure layers with developed porosity.[7,9] Carbon anode materials have unique advantages, such as an easy synthesis process; they can be prepared from any carbon-rich precursors, providing stable physicochemical/structural features, controllable porosity/pore features, high surface area, and good conductivity, which are requirements for suitable anode materials for commercial LIBs and NIBs.[10,11]

To date, several biomass precursors have been employed for the preparation of anodes for LIBs and NIBs, such as wood waste,[12] agro waste,[13,14] or industrial waste.[15] However, exploiting suitable anode materials for Na^+ storage has been a challenge mainly due to their larger ionic radius compared to Li^+, which causes a huge volume expansion during the intercalation process, resulting in their poor electrochemical performance against sodium.[6,8] Moreover, pure carbon anodes have issues related to limited capacities that hinder their application in the next generation of high-density energy batteries.

Combining the physicochemical properties of carbon and metal/metal oxides in one material is an efficient strategy for boosting the electrochemical performance of carbon anodes for LIBs and NIBs.[16–20] This strategy possesses several advantages, such as an easy processing methodology, tuneable microstructure and morphology, and flexibility in compositing with many types of high-energy density elements, such as post-transition metals and metal oxides, such as tin oxide (SnO_2).[20] Sn has both high electronic conductivity and theoretical capacity toward carbonaceous materials, and has great potential in the design of novel anode materials for LIBs and NIBs.[20,21] In addition, Sn has an electronegativity of 1.96, which is lower than that of carbon, which is 2.55. Therefore, changing the electron distribution will create an imbalance in the electronegativity and produce structural defects in carbon layers, which are the reaction sites for boosting its electrochemical properties and thereby enhancing its battery performances in NIBs.[21,22]

Huang *et al.*[22] prepared a series of carbon–Sn anodes for LIB applications, and they reported that compositing these elements generates a novel nanostructure that not only provides a high conductivity but also prevents aggregation of Sn nanoparticles, improving their overall cycling performance. Compared with pure SnO_2 and polypyrrole-derived carbon-coated hierarchical SnO_2, hierarchical SnO_2 with a double carbon coating composite exhibited 554.8 mA h g^{-1} for 50 cycles at 250 mA g^{-1} when tested against Li. In another study, Li *et al.*[23] reported a three-step process (involving two slow carbonization steps followed by hydrothermal carbonization) for preparing SnO_2/carbon anodes for NIBs. The as-prepared materials exhibited a reversible rate capability performance (149 mA h g^{-1} at 2000 mA g^{-1}) and long cycling performance (294 mA h g^{-1} after 150 cycles at 100 mA g^{-1}) against sodium.

Herein, we propose a facile strategy to synthesize a more sustainable biomass-carbon–SnO_2 nanostructured composite (denoted as BC/SnO_2) using phosphoric acid as the chemical activator. Phosphoric acid alongside zinc chloride and potassium hydroxide are some of the most used activating agents for the preparation of porous carbon materials. These chemical activators differ from each other, for example, KOH is known to create carbon materials with a widening of micropore width, while $ZnCl_2$ develops materials with more mesoporous features, and H_3PO_4 leads to a more heterogeneous pore size distribution.[24] H_3PO_4 has become a common chemical activating agent used for preparing carbon materials from a variety of starting materials, because of its lower environmental and toxicological constraints compared to $ZnCl_2$, and lower working temperature compared with KOH or NaOH.[25]

Anode materials' physicochemical properties have been deeply investigated using N_2 isotherms and porosity data, electron microscopy, Raman spectroscopy, and X-ray photoelectron spectroscopy (XPS). When employed as anode materials for LIBs and NIBs, the as-prepared BC/SnO_2 exhibited much improved specific capacities for both battery systems, highlighting that the incorporation of SnO_2 significantly enhanced the gravimetric capacities in half-cell configuration against alkali (Li/Na) metals validating the aforementioned analytical characterization techniques.

2 Materials and methods

2.1 Synthesis of carbon-based anodes

The birch biomass carbons were synthesized *via* two-step thermochemical processes.[11,26] Initially, 20 g of birch biomass (particle size lower than 500 μm) was mixed with 10 g of SnO_2, and nearly 80.0 mL of H_3PO_4 (25%) was added into a hydrothermal carbonization (HTC) vessel (150 mL of internal volume). The HTC vessel was placed inside an oven and heated up to 150 °C for nearly 16 h. After this procedure, the sample was cooled down and placed into a beaker and dried overnight at 105 °C. The dried sample was then pyrolyzed in an electric oven at 800 °C (ramped at 10 °C min^{-1}) for an hour under an inert atmosphere (N_2 flow of 50 mL min^{-1}). The reactor was allowed to cool down to room temperature. To eliminate any residual acid and Sn weakly attached to the carbon matrix, the sample was subjected to several washing processes (with agitation) with boiling water until the pH of the washing water was kept constant (close to neutral).[11,26] The sample was named BC/SnO_2. A similar procedure was used for the pristine carbon (BC), but without adding SnO_2.

2.2. Characterization of the carbon-based anodes

The specific surface area (SSA) values were obtained based on the Brunauer–Emmett–Teller (BET) method, while the pore size distribution curves were obtained from the Barrett–Joyner–Halenda (BJH) method. Transmission electron microscopy (TEM) images were taken using a Talos L120C microscope (FEI, Eindhoven, the Netherlands) at acceleration voltages of 200 kV. Raman spectra were obtained using a Bruker Bravo spectrometer (Bruker, Ettlingen, Germany). The samples were ground using an agate mortar and pestle and then scanned in the 300–3200 cm^{-1} spectral range. XPS analyses were performed using an ESCALAB™ 250Xi XPS system (Thermo Fisher Scientific, Waltham, USA). The measured data were analyzed using Avantage V5 software. Charge compensation was used to calibrate the binding energy (BE) by applying the C 1s line at 284.8 eV as a reference. Thermogravimetry (TGA) measurements were conducted on a STA6000 system under an air atmosphere, with the temperature range of 25–1000 °C at a consistent heating rate of 10 °C min^{-1}. Approximately 20 mg of BC and BC/SnO_2 were placed into the TGA reactor.

2.3 Electrode preparation and battery assembly

Slurries of BC/SnO_2 (80 wt%) and pristine BC (80 wt%) were prepared by mixing them with additive carbon (10 wt%; Super P, Alfa Aesar) and PVDF binder (10 wt%; MTI, USA) in NMP solvent separately. The uniform slurries were later coated onto copper foil (thickness ~10 μm) using doctor blade techniques and dried at 80 °C overnight. Then, the coatings were punched into 16 mm discs with a 2 cm^2 geometrical area, and active mass loading was found between 4–6 mg. Thus, the prepared electrodes were used as anodes to assemble coin cells (CR2032). The coin cell assembly was carried out inside an argon-filled glove box. Alkali metal discs (Li/Na) (thickness ~0.6 mm; MSE, USA) were used as counter/reference electrodes with respective electrolytes of 1 M $LiPF_6$ in EC/DMC (1/1 by volume, Sigma Aldrich) and 1 M $NaPF_6$ in EC/PC for LIBs and NIBs. A 19 mm disc of Whatman glass microfiber filter paper was used as a separator. The assembled coin cells were relaxed overnight before starting any electrochemical measurements.

2.4. Electrochemical measurements and characterization

Both BC/SnO_2 and control BC coin cells were tested at room temperature. First, cyclic voltammetry (CV) was conducted at a scan rate of 0.1 mV s^{-1} and in the voltage window of 0.005–3.0 V using a BioLogic SP-150e potentiostat. Next, galvanostatic cycling (charge–discharge) measurements were carried out at current densities ranging from 0.1C to 5C (1C = 372 mA^{-1}) in the voltage window of 0.005–3.0 V using a BioLogic BSC-800 series battery cycler. Potentiostatic electrochemical impedance spectroscopy (PEIS) measurements of the coin cells were made with an AC voltage pulse of 10 mV in a frequency range of 1.0 MHz to 1.0 MHz using BioLogic SP-150e. The impedance response of cells was measured at OCV after discharge and charged conditions. The data obtained fit into Nyquist plots and corresponding equivalent circuits using ZView software. The charge–discharge cycling of all sodium cells was tested between 0.002 and 3.0 V using an Arbin multichannel battery tester (USA) and BioLogic VMP3 tester (France).

2.5 Computational methods

In this paper, the GFN1-xTB method[27] in conjunction with the supercell approximation was applied as implemented in the DFTB+ package.[28] GFN1-xTB is an elegant formalism based on the DFTB method[29] that allows for a detailed electronic description of different systems using sets of global and element-specific parameters. GFN1-xTB employs minimal basis sets of atom-centered orbitals and involves only valence electrons (frozen core approximation). The dispersion energy is computed using the D3 method.[30] The geometry optimizations were performed until the maximum force on each atom was lower than 0.01 eV $Å^{-1}$. The self-consistent charge convergence criteria (SCC tolerance) was 10^{-7} for static calculations and 10^{-5} for molecular dynamic (MD) simulations. We used a Fermi distribution filling with an electron temperature of 100 K to facilitate convergence. The Brillouin zone of the BC and BC/SnO_2 supercells was sampled with a Monkhorst–Pack *k*-point mesh[31] of 6 × 6 × 1 for static calculations and of 1 × 1 × 1 for MD simulations. Our test calculations showed that the energy difference between both *k*-point settings was less than 0.06 meV per atom. The peak width for broadening was set to 0.1 eV, which is better for visualizing the density of states (DOS) plot. The amorphous carbon structure (denoted as BC) was taken from ref. 32 which provides a library of structures at different system sizes obtained by combining machine learning and density functional theory (DFT). The supercell representing BC contained 512 atoms with the lattice constants equal to a = 15.055 Å, b = 15.055 Å, and c = 40.0 Å, and with the vacuum space around 24 Å. The tin oxide (denoted as SnO_x) was represented by the $Sn_{10}O_{16}$ cluster. To analyse the structural rearrangements of BC/SnO_x in real time and at finite temperatures, GFN1-xTB MD simulations were performed. The velocity-Verlet algorithm with a time step of 1.0 fs was selected to integrate the Newton equations of motion. The temperature was controlled using a Nosé–Hoover chain[33] thermostat (chain-length of 3). Our theoretical protocol was based on simulated annealing,[34] where by heating up a system, and then allowing it to cool slowly, stable minima can be found. The whole procedure involved three phases: initial heating of the system from 1 K to 1100 K over a period of 4 ps, then further equilibration at 1100 K for 2 ps, and cooling to 300 K for 4 ps (see Fig. 8). Finally, the obtained structure was optimized to analyze its electronic properties. Initially, we also performed this protocol for BC and the $Sn_{10}O_{16}$ cluster in the gas phase to check their stability at 1100 K.

3 Results and discussion

3.1. Physicochemical features of the BC and BC/SnO_2 anode materials

The porosity characteristics of the anode materials play a significant role in the electrochemical performance of the electrode materials. Hence, N_2 isotherms and pore size distribution data

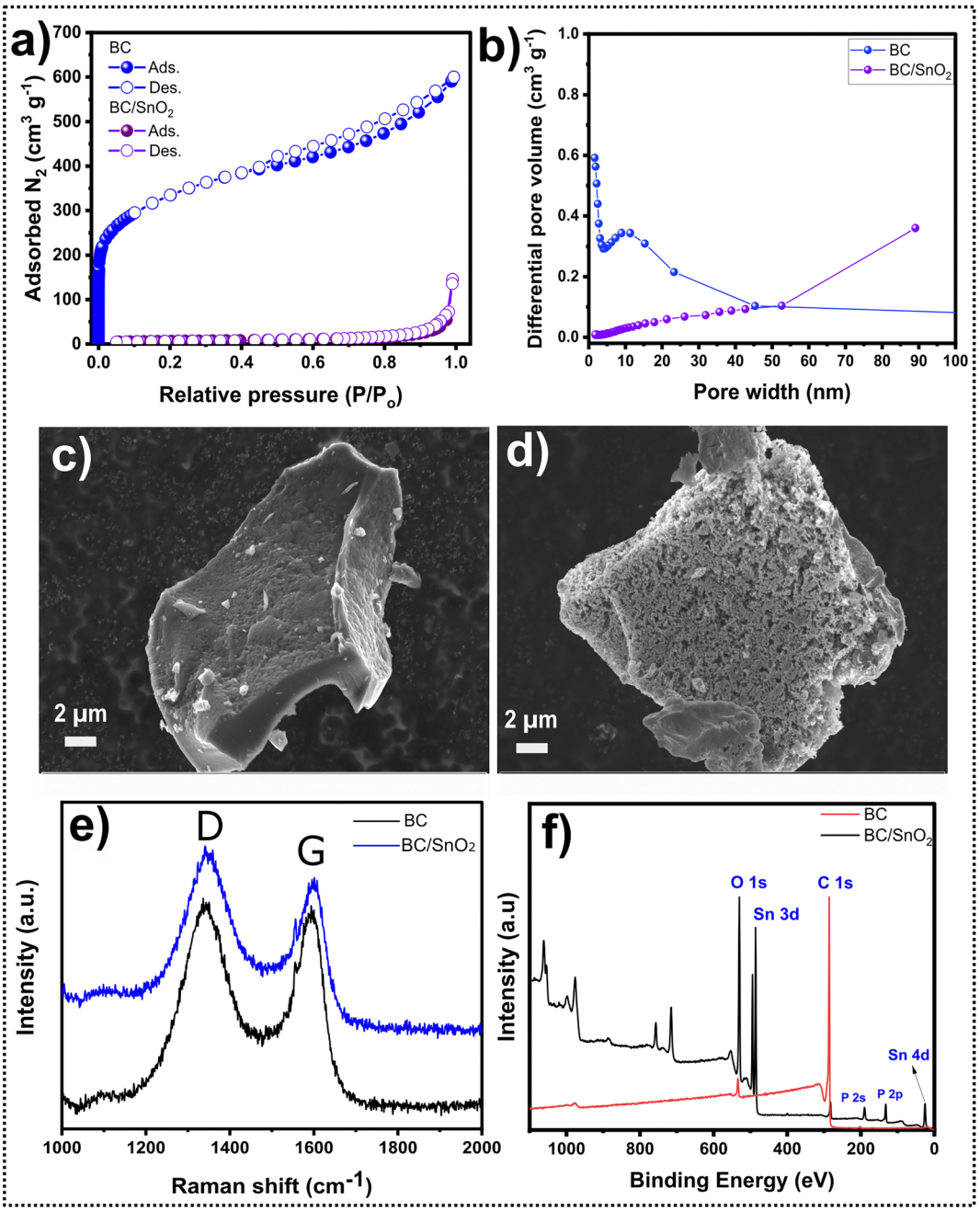

Fig. 1 (a) N_2 isotherms of adsorption–desorption, (b) pore size distribution curves, (c) SEM image of BC at 10$k\times$ magnification, (d) SEM image of BC/SnO_2 at 10$k\times$ magnification, and (e) Raman and (f) XPS spectra of the BC and BC/SnO_2 samples.

of the BC and BC/SnO_2 are shown in Fig. 1a to investigate their porosity characteristics. Fig. 1a displays highly different isotherm curves. According to the IUPAC classification,[35] the N_2 for the BC material could be classified as a combination of Type I, due to the N_2 uptake at low partial pressure (suggesting the presence of micropores), and Type IV (due to the presence of mesopores), which is evidenced by the prominent presence of hysteresis. Meanwhile, for BC/SnO_2, the curve seems to be Type III (of nonporous or macroporous features). This kind of significant difference between both isotherms could be because the introduction of Sn into the BC structure led to pore blocking, which can reduce its specific surface area (SSA). The values of the SSA were 1159 $m^2\ g^{-1}$ for BC and 24 $m^2\ g^{-1}$ for BC/SnO_2. The pore structure of the anodes was further analyzed by the pore size distribution curves (Fig. 1b). As shown in the N_2 isotherms, both materials show extremely distinct pore structures. In BC, there is a wide range of pore sizes, such as high amounts of micropores and small mesopores (1.7–5 nm) and mesopores in the range of 5–45 nm. In addition, small quantities of macropores in the 50–100 nm range were also found in BC. However, in BC/SnO_2, almost a macropore centered in the size of 90 nm is seen (refer Fig. 1b). These results are consistent

with the N_2 isotherms, and differences in their pore sizes can have a positive impact on the electrochemical performance of both materials. This is due to the well-known fact that mesoporosity can provide sufficient space and efficient transport channels for Li and Na ions. However, the presence of macropores could also be beneficial, enabling faster ion and electron transports.[36] Moreover, macroporous structures can better alleviate the volume change of the anode due to intercalation of metal ions (Li^+/Na^+).[37]

The morphological features of BC and BC/SnO_2 were examined by SEM to evaluate the impact of the Sn incorporation into the BC structure (Fig. 1c and d). The morphologies of the BC sample (Fig. 1c and Fig. S1a, ESI†) and BC/SnO_2 (Fig. 1d and Fig. S1b, ESI†) are shown. The SEM morphology images were taken at 10$k\times$ and 50$k\times$ magnifications. The introduction of Sn had a remarkable impact on the surface morphology of the BC sample. Pristine BC seems to exhibit a smoother surface with no cracks or holes (Fig. 1c). However, the same image at 50$k\times$ magnification (Fig. S1a, ESI†) reveals a surface that is extremely rough and rich in small holes, which indicates a large number of small pores, in accordance with the previous porosity data. Compared to BC, BC/SnO_2 displays a significantly different morphology (Fig. 1d and Fig. S1b, ESI†). BC/SnO_2 displays a much rougher and irregular surface with the existence of bigger holes/pores (Fig. 1d and Fig. S1b, ESI†), which can be attributed to the surface agglomeration of Sn. Fig. S2 (ESI†) displays the EDX mapping for oxygen and Sn, which revealed a homogeneous distribution of Sn over the BC structure, suggesting an efficient mix/compositing between these two elements. Such homogeneous distribution could positively impact the even charge distribution over the BC/SnO_2 anode structure by facilitating and shortening ion diffusion. The quantitative EDX analysis indicated that around 5.1 at% of Sn was incorporated in the BC structure, proving its successful modification.

Raman spectroscopy was performed to examine the Sn incorporation effect on the degree of order/disorder and graphitization degree of the BC and BC/SnO_2, as shown in Fig. 1e. A typical Raman spectrum of biomass-derived carbon exhibits characteristic signatures related to G and D bands centered at $\sim$1346 and 1600 cm^{-1}, respectively.[11,12,38] The G band suggests the presence of a graphitic structure in the carbon network, while the D band indicates structural defects in the carbon lattice. At first glance, the Raman spectra of both materials are very similar. However, I_D/I_G was calculated for further evaluation.[39–41] A smaller I_D/I_G value indicates that the material possesses a more ordered graphitic structure with an elevated graphitisation degree, while a higher I_D/I_G value indicates that the material is richer in defective carbon lattice structures. In this sense, BC has an I_D/I_G value of around 1.5, while BC/SnO_2 has a value of 1.8. This clearly suggests that the incorporation of Sn created a material (BC/SnO_2) with more structural defects in the carbon structure.

The results so far have shown that the physical and morphological structures of the BC and BC/SnO_2 are very distinct. However, the chemical structure of the materials also needs to be evaluated. In this sense, the surface chemistry and elemental composition of BC and BC/SnO_2 were investigated by XPS to observe the impact of Sn incorporation on BC surface/structure. The XPS survey spectra of both BC and BC/SnO_2 (see Fig. 1f) revealed the apparent presence of C, O, and P in BC and BC/Sn. In contrast, a high content of Sn (8.9 at%, atomic percentage) is seen in BC/SnO_2, suggesting the successful incorporation of Sn atoms in the BC structure. It is worthwhile mentioning that since Sn was detected with different binding energies (in eV), it suggests Sn is found in different oxidation states, since Sn was observed only in BC/SnO_2, and its deconvoluted spectrum is shown in Fig. S3a (ESI†). Two peaks are seen, which are related to the Sn 3d spectrum, at 497.2 eV (Sn $3d_{3/2}$) and 488.3 eV (Sn $3d_{5/2}$). Furthermore, the valence band spectrum of BC/SnO_2 (Fig. S3b, ESI†), suggests that SnO_2 is the main form of Sn in BC/SnO_2.[42,43]

Fig. 1f also highlights the presence of phosphorus in both samples. It is worthwhile noting that the P is present in PO_4^{3-} form (3.8 at%, BC/SnO_2, and 1.3 at% for the BC sample), and it comes from H_3PO_4 that was used to chemically activate carbon materials. The presence of P can improve the surface reactivity and wettability of carbon materials, and improve their electrical conductivities, whereas all these characteristics can contribute to trigger faradaic redox reactions between electrode–electrolytes, which enhance the battery's performance.[44–46]

The microstructures of the BC and BC/SnO_2 materials were further examined by HRTEM (Fig. 2). Obvious differences are observed, highlighting that the Sn incorporation affected the inner structure of the carbons. The TEM image of BC (Fig. 2a) suggests a porous structure by the BET data, with a dominant amorphous structure.[41] The BC/SnO_2 shows less porous and more densely packed (aggregated) structures (Fig. 2c), also with a dominant amorphous phase. Some aggregates together may form big inter-particle pores, which may facilitate the wetting of electrolytes and the diffusion of ions.[38] STEM-EDX was employed to further evaluate the effect of the Sn on the structure of carbon materials and observe the main elemental distribution of the elements (Fig. 2b and d). The BC exhibited only carbon, oxygen, and phosphorus in its structure (Fig. 2b), BC/SnO_2 displayed homogeneously distributed Sn, O, and P elements, confirming that the Sn-compositing strategy had succeeded. Such homogeneous Sn distribution onto the carbon is expected to boost its electrochemical properties because it facilitates the interfacial electrochemical reactions of solid–electrolyte interfaces.[16,17,47]

The thermogravimetric (TGA) analysis of BC and BC/SnO_2 was carried out in air to compare their thermal stabilities and mass losses (see Fig. S4, ESI†). The TGA profiles for both samples indicate that the BC sample was completely decomposed at 1000 °C, while BC/SnO_2 exhibited a mass loss of 43.0%, which is attributed to the carbon component, and thus it can be concluded that the BC/SnO_2 consists of approximately 43.0% of carbon content by weight.[48,49]

3.2. Electrochemical performance of the anode materials in LIBs

The electrochemical features of the BC and BC/SnO_2 anodes were investigated by CV analysis. Fig. 3a shows typical CV

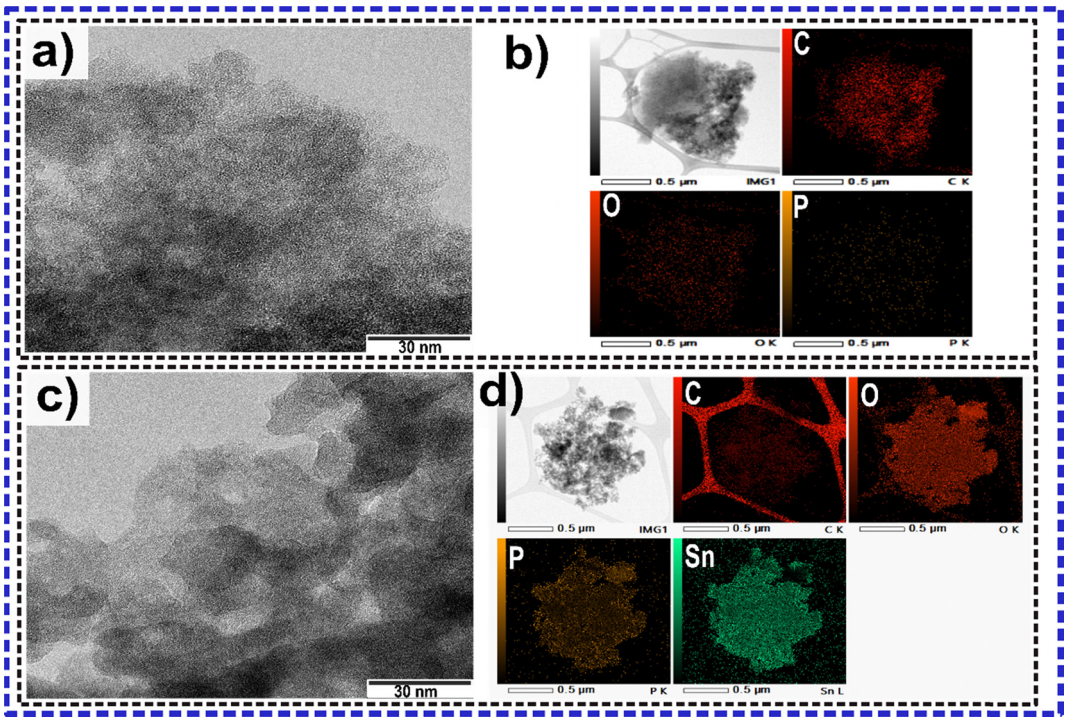

Fig. 2 HRTEM images of (a) BC and (c) BC/SnO_2, and their corresponding STEM-EDX maps, (b) BC and (d) BC/Sn.

curves of the amorphous carbon derived from biomass resources (BC).[12,50] In the first cycle, the broad reduction peak near 1.0 V is related to the irreversible formation of a solid electrolyte interface (SEI) due to electrolyte decomposition on the surface of the BC electrode.[12,50] This reduction peak is not seen in the subsequent cycles, suggesting that the SEI formation mostly occurred at the first cycle, which may cause a loss of capacity after the first cycle. Moreover, the CV profiles seem to almost overlap with each other, which may indicate that the Li^+ insertion/de-insertion exhibited good reversibility and the excellent electrochemical stability of BC.

BC/SnO_2 clearly showed different CV profiles with evident faradaic contributions compared to BC. In Fig. 3b, for the CV curve of the BC/SnO_2 anode, the broad peak at 1.25 V could be related to the conversion reaction between Li^+ ions and SnO_2 as per eqn (1) and (2), as well as the intercalation of Li^+ ions into the carbon network.[50–52] The broad cathodic peak between 1.0 and 0.5 V could be related to SEI formation, which is irreversible due to its absence in the subsequent cycles.[22,51] An alloying reaction between Li^+ ions and Sn occurs below 0.5 V as per eqn (3).[52,53] The CV curves show two anodic peaks, ~0.4 and ~1.25 V, among which the earlier peak becomes more discernible with the cycling. The peak at ~0.4 V is due to the reversible de-alloying reaction of Li_xSn, resulting in pure Sn formation as per eqn (3).[54] The peak at ~1.25 V can be attributed to the oxidation of Sn to SnO, as per eqn (2). Further oxidation of SnO to SnO_2 as described in eqn (1), takes place above 1.8 V like the broad hump observed around 2.0 V. It is reported that this reaction is also capable of additionally increasing the capacity of the electrode material.[55] Moreover, the CV curves have closely overlapped each other after the second cycle, which indicates that the LIB with BC/SnO_2 provided good reversibility in the Li^+ intercalation/deintercalation process. From the CV, it can also be extracted that the redox couples of Li_xSn ($\leq$0.5 V) and SnO_2 ($\geq$1.25 V) persisted in all cycles, which suggests good reversibility of the BC/SnO_2 electrode.[56] This good reversibility is not possible with pure SnO_2 anodes, as reported in the literature, due to huge volume changes of both Sn and SnO_2 phases upon lithiation that cause early-stage failure of the electrode materials. Compositing SnO_2 with BC seems a good remedy to avoid this kind of failure as well as to exploit the high lithiation potential of SnO_2. The multipurpose role of BC, *i.e.*, it buffers the volume changes and acts as an efficient current collector and it has the ability to store Li-ions, enables good reversibility of the conversion of SnO_2 and subsequent Sn alloying reactions.

$$SnO_2 + 2Li^+ + 2e^- \rightleftharpoons SnO + Li_2O \quad (1)$$

$$SnO + 2Li^+ + 2e^- \rightleftharpoons Sn + Li_2O \quad (2)$$

$$Sn + xLi^+ + 4e^- \rightleftharpoons Li_xSn \quad (0 \leq x \leq 4.4) \quad (3)$$

Fig. 3c and d show charge–discharge curves of BC and BC/SnO_2 at 1.0C, respectively. The first discharge curve consists of two slope regions and a plateau, in accordance with the broad peaks observed during the CV scans. For the BC anode, the first charging and discharging cycle had a specific discharge capacity of 499.3 mA h g^{-1}, while for charging, it was only 73.4 mA h g^{-1}, resulting in an initial 15% Coulombic efficiency (CE). For BC/SnO_2, the specific discharge capacity

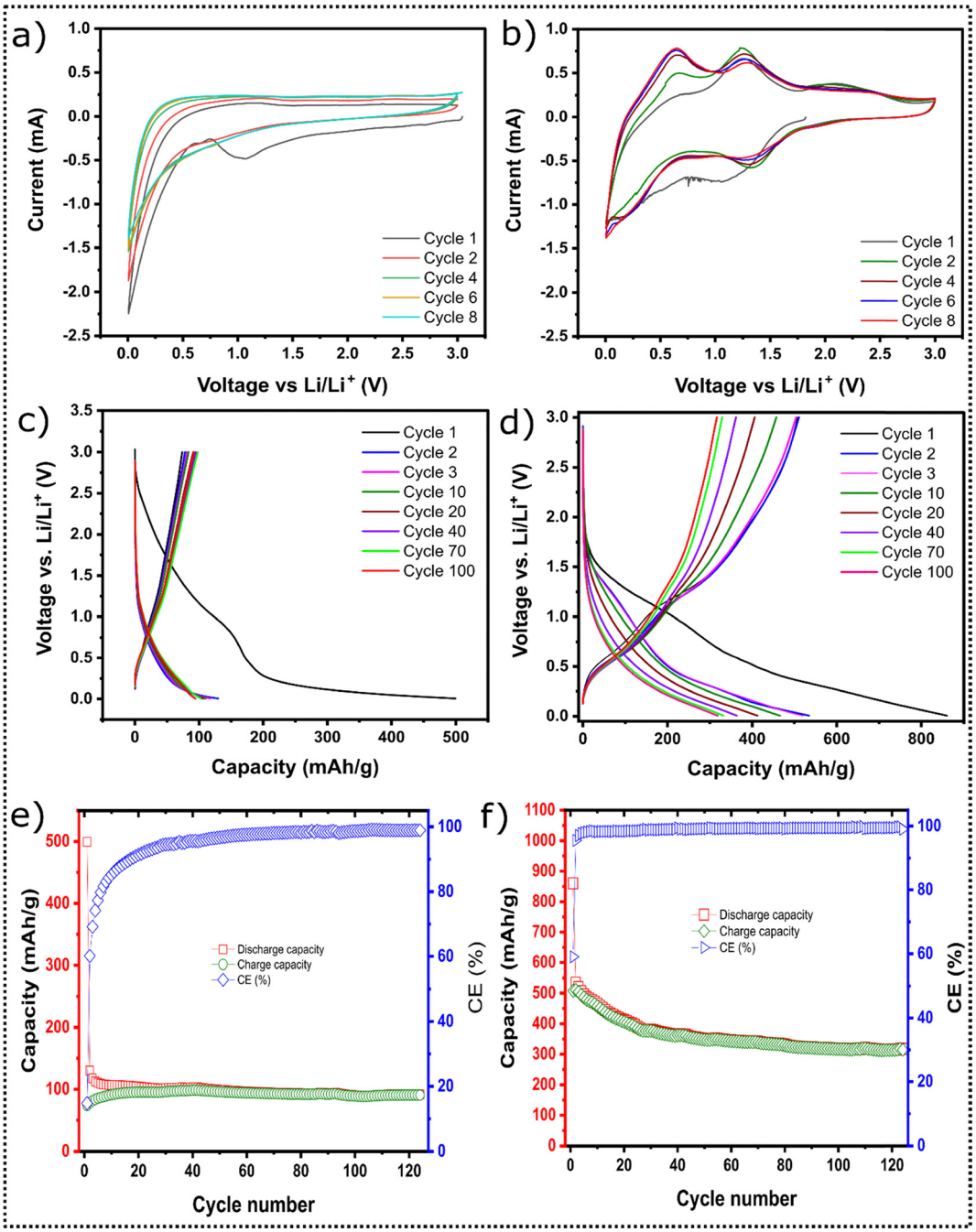

Fig. 3 Cyclic voltammetry curves of (a) BC and (b) BC/SnO_2; charge and discharge curves of (c) BC and (d) BC/SnO_2; cycling performance of (e) BC and (f) BC/SnO_2 at 1C.

was 1066 mA h g^{-1}, while for charging it was 698 mA h g^{-1}, resulting in an initial CE of 65.5%. Such low initial CE can be attributed to the SEI formation and a partially irreversible alloying reaction between C and Li (for BC anode), and Sn and Li for BC/SnO_2.[54] From the second cycle, the BC/SnO_2 anode started to exhibit very good cycle stability, and the specific capacity remained above 319 mA h g^{-1} at the end of 120 cycles (see Fig. 3f). At the same time, its CE is also greatly improved, reaching 98%, indicating the good cycling stability of the BC/SnO_2 anode. However, the BC anode exhibited a capacity of 93.2 mA h g^{-1} at the end of 120 cycles (see Fig. 3e), highlighting the much better performance of the BC modified with SnO_2. The electrochemical metric of the BC/SnO_2 was further improved when submitted to cycling at 0.1C (see Fig. S5, ESI†), and exhibited a capacity of 453 mA h g^{-1} at the end of 120 cycles.

Fig. 4 exhibits the rate performance of both BC and BC/SnO_2 anodes at different current densities. The capacity's decrease at high current densities could be related to the fact that redox reactions are maximized on the material's surface at faster

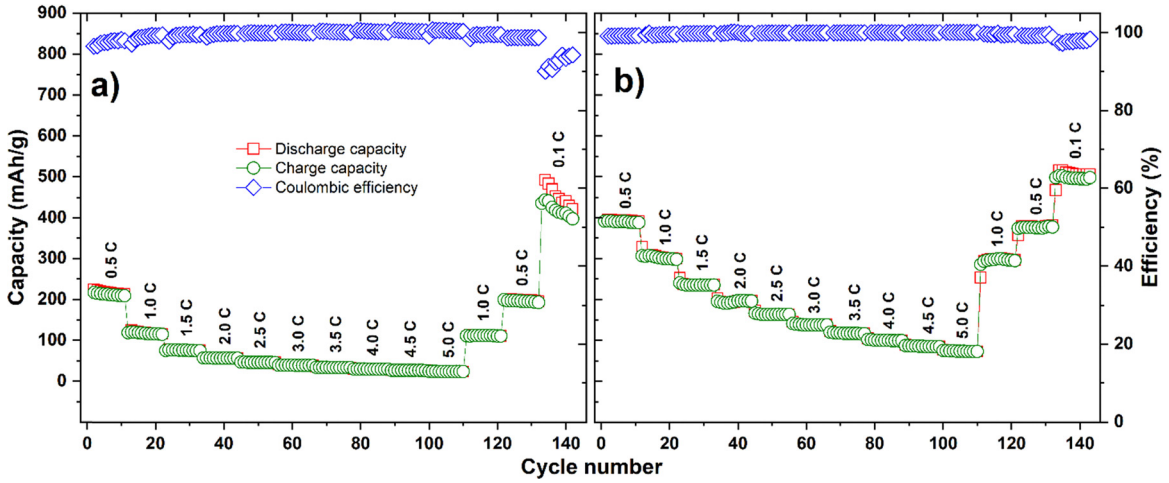

Fig. 4 Rate capability test of lithium cells bearing, (a) BC and, (b) BC/SnO_2 electrodes under various C-rates.

charge–discharge rates,[21] which is also known as the C-rate effect,[52] which prevents the active sites of electrode active materials from fully participating in the reaction. However, the anode's capacity shows an upward trend when it is subjected to a lower value. After 140 cycles, the BC anode sample exhibited a higher instability, showing a capacity decay (Fig. 4a) and lower CE compared to BC/SnO_2, which retained excellent capacity, fully recovered, and good CE. Fig. 4b exhibits the rate capability performance of the BC/SnO_2 composite at different rates. The specific capacity of BC/SnO_2 decreased from 391.1 mA h g^{-1} at 0.5C to 85.1 mA h g^{-1} at 5.0C and recovered to 377.2 mA h g^{-1} at 0.5C at the end of 132 cycles. Such results strongly suggest that BC/SnO_2 can keep its specific capacity stable at the different current densities and it can even return back to a significant specific capacity when it is tested again at 0.5C. Moreover, in the rate test at the end of 143 cycles at a C-rate of 0.1, the BC/SnO_2 returned to a capacity of 397.3 mA h g^{-1}, which exhibits its outstanding capacity reversibility. With the above analysis, the cycle stability of the BC/SnO_2 sample material has proven excellent.

To further evaluate aspects related to the Li-ion intercalation into BC and BC/SnO_2 anodes, PEIS was performed, and the impedance response plotted as Nyquist plots are shown in Fig. 5. Fig. 5a and b show typical semicircles whose diameter in the high-frequency region is generally associated with the resistance to charge transfer, while the inclined line in the low-frequency region indicates the Li-ion diffusion process. Comparing both electrodes, the semicircle's diameter at open-circuit-voltage (OCV), is slightly smaller for BC/SnO_2 (see Fig. 5a) than of that of the BC electrode (see Fig. 5b), demonstrating that the resistance to charge transfer decreased with the Sn incorporation into the carbon matrix. In addition, the BC/SnO_2 anode displayed less resistance to charge transfer compared to the BC anode since BC/SnO_2 seems to allow a more free movement of charges, plausibly due to the enhanced conductivity provided by the Sn atoms in the carbon matrix, which improved the electron transport efficiency during the Li-ion intercalation/deintercalation process.

To further evaluate the lithiation/delithiation kinetics, the Nyquist plots are fitted into the equivalent circuit (EC) of each

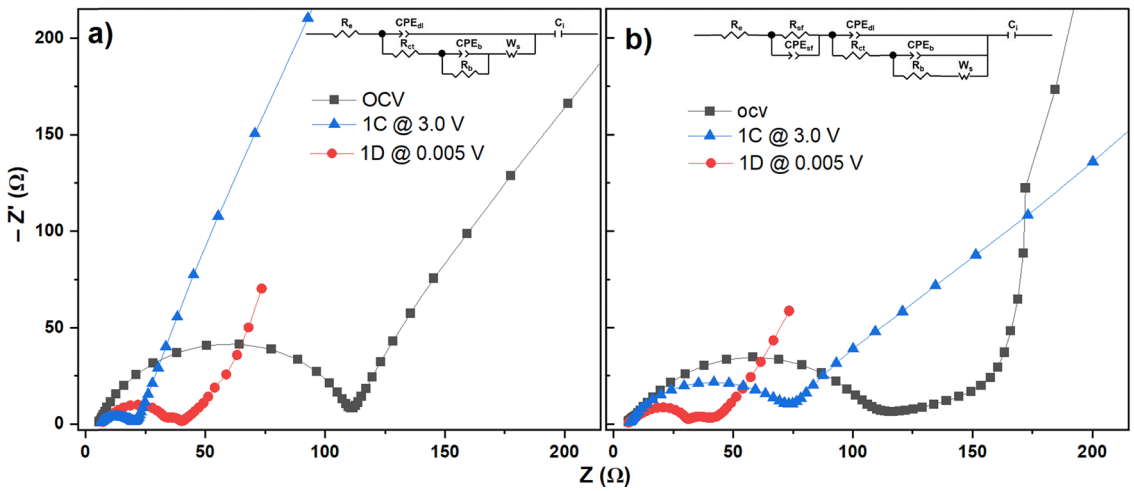

Fig. 5 (a) Nyquist plots for the BC/SnO_2 electrode and (b) Nyquist plots for the BC electrode.

system (BC and BC/SnO_2) as shown in Fig. 5a and b (inset). From the ECs, parameters such as the contact resistance (R_e), resistance to charge transfer (R_{ct}), resistance due to surface film formation (R_{sf}), and bulk resistance (R_b) are calculated as seen in Table 1.[57–60] The lower R_{ct} values of BC/SnO_2 strongly suggest its significant improvement in the electron-transfer kinetics compared to the BC sample. Furthermore, the R_{ct} values continuously decreased from OCV to discharge and to the charge state for BC/SnO_2 whilst increasing for BC from discharged to charged state, once again proving the superior electrical property of the BC/SnO_2 anode. It is worth noticing that the R_b value of BC/SnO_2 was found to be twice the R_{ct} value, at least in all three states of charge conditions. The condition of $R_b > R_{ct}$ suggests redox reactions taking place at very fast rates, and the BC/SnO_2 behavior is towards the ideal conductor.[57,60] On the other hand, BC exhibited $R_b < R_{ct}$ indicating the superiority of BC/SnO_2. In general, R_b originates from the electronic conductivity of the electrode matrix, copper substrate, and ionic conductivity due to the electrolyte present in the pores of the active material and composite electrode matrix.[57,60] Furthermore, R_{sf} is found in both anode cases only in the discharged states but its value for BC/SnO_2 is found to be lower than that for BC. The *in situ* formation of ultrafine nanoparticles of Sn/SnO_2 due to electrochemical rupturing and reconstruction that further lead to electrolyte polymerisation as seen in the MnO/GNS case could be plausibly behind the observed R_{sf}.[52,53] In the case of BC, excessive electrolyte decomposition *i.e.* high extent of SEI formation due to the high SSA as seen in BET analysis could be the origin of R_{sf}. Our results highlight that the BC/SnO_2 composite not only enables a much better electrical conductivity but also facilitates the reversible Li-ion diffusion kinetics, which lead to a high charge/discharge capacity and excellent rate capability.

3.3. Electrochemical performance of the anode materials in NIBs

Na^+ has an electrochemical standard reduction potential higher (−2.71 V) than Li^+ (−3.04 V); it has a higher atomic mass and tends to exhibit slower insertion kinetics. Thus, NIBs deliver a lower energy density than LIBs when the same materials are tested. In this section, BC and BC/SnO_2 are also tested in sodium half cells for NIBs. To evaluate the electrochemical activity of BC and BC/SnO_2 anodes towards the Na^+ storage process, Fig. 6 shows the CV curves at a scanning rate of 0.1 mV s^{-1} within the voltage window from 0.002 to 3.0 V. The CV curves show remarkable differences. The BC curve (Fig. 6a) exhibits a typical capacitive behavior observed for activated carbon with no evident redox peaks.[12,61] However, for the BC/SnO_2 anode, evident faradaic contributions are observed (Fig. 6c). Firstly, both anodes clearly show a broad peak from 1.0 to 0.002 V in the first cathodic scan, which is associated with the combined effectiveness of the reaction between the Na^+ and BC functionalities, and Na^+ and Sn presented in BC/SnO_2 and consequent formation of the SEI film. Moreover, for both samples, the CV curves almost overlapped after the second cycle, indicating that both anodes provided good stability/reversibility in the Na^+ storage process. A cathodic peak around 0.75 V is observed in BC/SnO_2, suggesting an alloying reaction between Na^+ ions and Sn to form the Na_xSn alloy, into a carbon network.[62–64] Moreover, the CV curves for BC/SnO_2 exhibited two anodic peaks (~0.55 and ~1.5 V, respectively), which correspond to the desodiation process of the $Na_{15}Sn_4$ alloy, specifically, to the Na_9Sn_4, $Na_{15}Sn_4$, $NaSn_5$, and NaSn,[62–64] which are in accordance with the findings reported elsewhere.[65]

The performances of the BC and BC/SnO_2 anodes in NIBs were further evaluated by galvanostatic methods for different cycling numbers (Fig. 6b and d). The initial discharge capacity for the BC anode was 1326 mA h g^{-1} with an initial CE of 21.2% indicating strong side reactions leading to irreversible SEI formation. In the second cycle, the capacity was 339 mA h g^{-1} with 77.0% CE, indicating capacity fade or irreversible loss. For the BC/SnO_2 anode, the first cycle gave a discharge capacity of 705 mA h g^{-1} with a 52.1% initial CE, and a second cycle presented a discharge capacity of 373 mA h g^{-1}, exhibiting 92.2% reversibility and maintaining its very high performance at the end of 150 cycles, which shows its excellent electrochemical stability.

Fig. 7a shows the rate test performances of these anodes. When comparing the reversible capacity between BC and BC/SnO_2 at different current densities, the BC/SnO_2 composite has a higher performance. Increasing current densities from 25 mA g^{-1} to 1000 mA g^{-1}, the reversible capacities of the BC/SnO_2 continuously dropped from 322 mA h g^{-1} to 61 mA h g^{-1}, respectively. However, when the current returned to a low current, BC/SnO_2 recovered fairly well with a high capacity; for instance, at 250 mA g^{-1}, the capacity of BC/SnO_2 recovered to reach 174 mA h g^{-1}, highlighting a gain in relation to the previous value (130 mA h g^{-1}), also exhibiting excellent capacity reversibility. The rate tests also showed that BC has a similar behavior at high current density but low capacity at medium and low current. The above results show that BC/SnO_2 outperforms pure BC regarding rate performance and capacity.

To further evaluate the carbon-based anodes in NIBs, the anodes were subjected to a long cycling stability experiment at 100 mA g^{-1} (see Fig. S6, ESI†). BC/SnO_2 exhibited better cycling stability, giving a higher capacity during all cycles compared to the BC anode, delivering a capacity of 204 mA h g^{-1} at the end of 162 cycles, while BC delivered a capacity of 165 mA h g^{-1}.

Table 1 PEIS data fit results for SIBs of BC and BC/SnO_2 B electrodes under different charge–discharge conditions

	R_e (Ω)	R_{ct} (Ω)	R_b (Ω)	R_{sf}
BC/SnO_2				
OCV	6.01	105.7	334.6	—
1D@0.005 V	7.19	21.2	8.11	4.59
1C@3.0 V	3.03	18.33	41.34	—
BC				
OCV	7.78	103.6	52.6	—
1D@0.005 V	6.35	17.25	11.2	7.27
1C@3.0 V	6.93	66.50	436.7	—

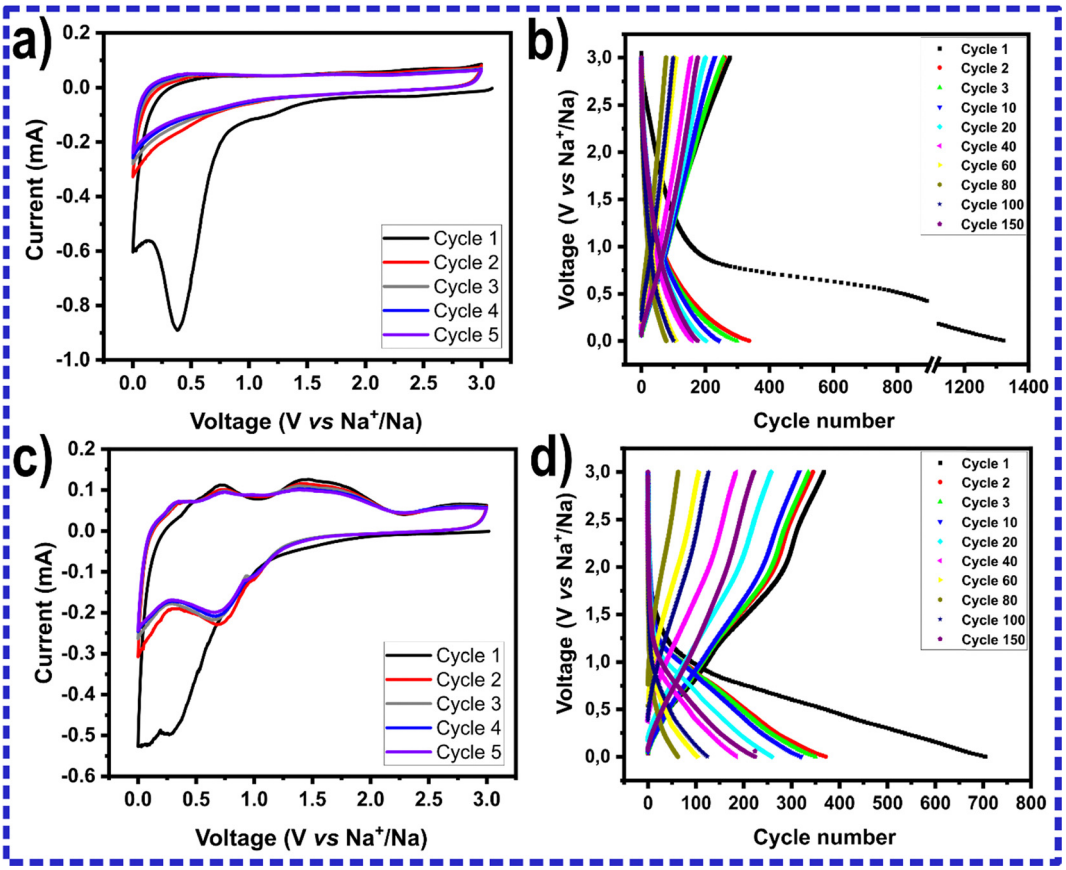

Fig. 6 (a) Cyclic voltammetry curves of the BC anode and (b) charge and discharge curves at different cycles for the BC anode, (c) cyclic voltammetry curves of the BC anode and (d) charge and discharge curves at different cycles for the BC/SnO_2 anode (NIBs).

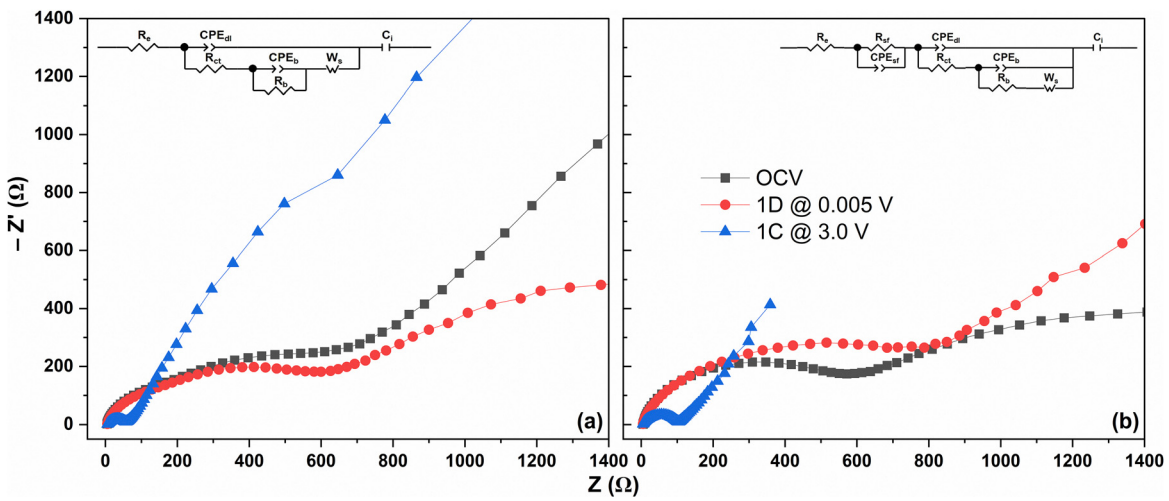

Fig. 7 EIS and Nyquist plots of reversible sodium storage for BC/SnO_2 (a) and BC (b) anodes (inset: equivalent circuit).

This can be clearly attributed to Sn incorporation and the macroporosity features that help fast ion transport and improve electronic conductivity.[12,22]

The further evaluation of the sodiation/desodiation process was assessed by PEIS. Nyquist plots, which are fitted into EC of each system (BC and BC/SnO_2) as shown in Fig. 7a and b (insert). From the ECs, the R_e, R_{ct}, R_{sf}, and R_b values were also determined as previously demonstrated for LIBs (see Table 2). BC/SnO_2 displayed lower R_{ct} values for all three states of charge investigated, OCV, full discharged, and full charged cycles

Table 2 EIS data of BC/SnO_2 and BC electrodes under different charge–discharge conditions

	R_e (Ω)	R_{ct} (Ω)	R_b (Ω)	R_{sf}
BC/SnO_2				
OCV	6.01	105.7	334.6	—
1D@0.005 V	7.19	21.2	8.11	4.59
1C@3.0 V	3.03	18.33	41.34	—
BC				
OCV	7.78	103.6	52.6	—
1D@0.005 V	6.35	17.25	11.2	7.27
1C@3.0 V	6.93	66.50	436.7	—

(see Table 2), potentially enhancing the charge transfer, suggesting that SnO_2 incorporation significantly improved the electron-transfer kinetics compared to the BC anode. Furthermore, the R_{ct} values decreased from OCV to discharged and to charged state. From the R_{ct} values, we can state the superiority of the BC/SnO_2 anode compared to the BC anode. R_b values are also lower for BC/SnO_2 than BC, attributing to its better electronic conductivity. Regarding R_{sf}, it is found only for the BC anode, and the lack of R_{sf} for BC/SnO_2 strongly corroborates its electrochemistry superiority, and the presence of SnO_2 may have led to less electrolyte decomposition, which ends in a thinner SEI compared to the BC anode. Therefore, the incorporation of SnO_2 into carbon was an efficient strategy to produce an anode with much better reversibility and Na^+ diffusion kinetics, which lead to a high charge/discharge capacity and excellent rate capability, as also shown in LIBs. The PEIS results support the improved electrochemical performance of BC/SnO_2 for LIBs and NIBs.

3.4 Electronic properties of BC/SnO_x

Understanding the structure, electrochemical properties, and reactivity of the amorphous BC/SnO_x system towards Li and Na ions is a very complex issue including many different aspects. Therefore, we focused here only on comparing electronic properties of BC/SnO_x and BC. In a real mixed system, a variety of mutual connections exist between both components, *i.e. via* faces, edges, corners, and defects. Therefore, including these

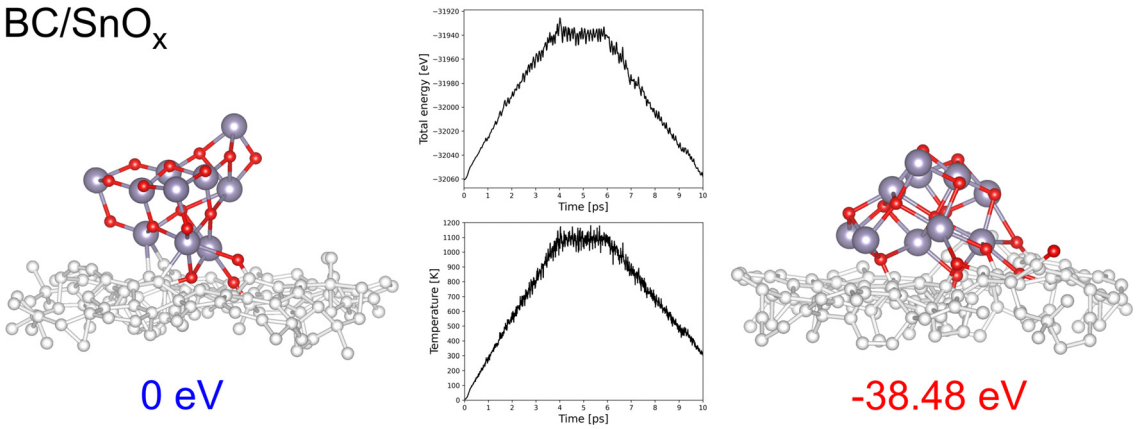

Fig. 8 The initial and final structure of BC/SnO_x after the geometry optimization. The changes in the total energy of the system and the corresponding temperatures are presented. Carbon atoms are white, tin atoms are lilac and oxygen atoms are red. The deeper carbon layers are not shown for transparency.

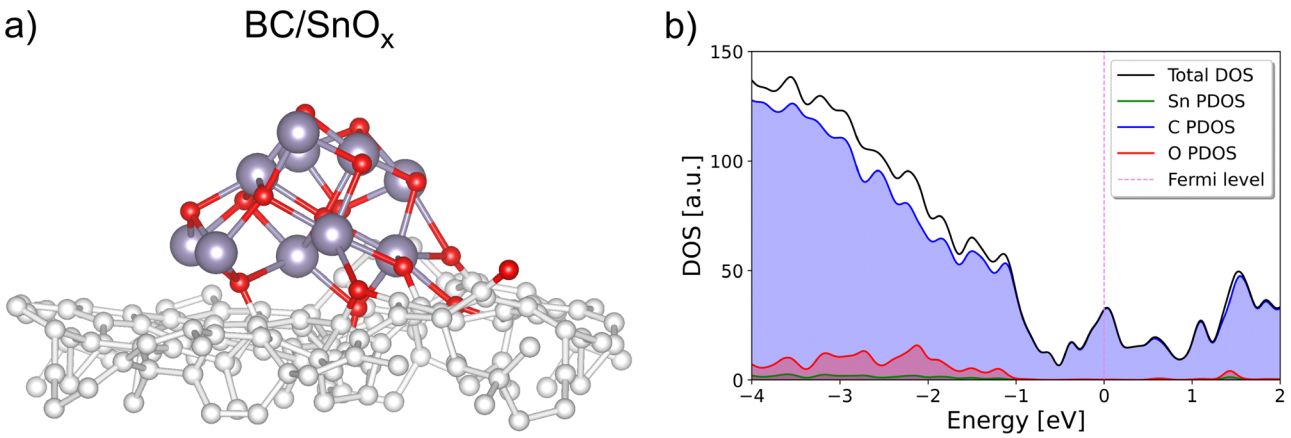

Fig. 9 (a) Side view of the relaxed structure of BC/SnO_x with the corresponding (b) total and projected density of states (DOS) obtained from the GFN1-xTB calculations. Carbon atoms are white, tin atoms are lilac and oxygen atoms are red. The deeper carbon layers are not shown for transparency.

cases would lead to an extremely large supercell with thousands of atoms. On the other hand, DFT calculations are limited to relatively small systems and easily become prohibitively expensive for large systems. Therefore, we applied the semiempirical GFN1-xTB method,[27] as a reasonable compromise between accuracy and computational cost. The supercell representing amorphous carbon that mimics the BC structure was taken from ref. 32, while the stable mixed BC/SnO_x system was obtained based on the simulated annealing procedure (see details in Section 2.5, and Fig. 8).

We found that SnO_x is attached to the surface of BC *via* eight Sn–O–C links, see Fig. 9a. Two O atoms built into the BC surface form altogether four bonds with C atoms equal to 1.39–1.45 Å, whereas a further four O–C bonds are contained in the range of 1.23–1.35 Å. Furthermore, in one case, the isolated carbonyl bond was created (1.20 Å). The obtained distances of O–Sn were found to range from 1.97 to 2.61 Å. Interestingly, the direct Sn–C bonds do not form in the mixed system. Finally, we analyzed the electronic structure of BC/SnO_x. In Fig. 9b, the total and projected DOS of the mixed system is shown with the Fermi level set to 0 eV. The plot is limited to the energy range, including the top of the valence band (VB) and the bottom of the conduction band (CB). In the mixed system, the Sn and O bands extend to around −1.1 eV in the VB and they barely exist in the CB (in the considered range). However, the area close to the Fermi level consists only of the C states. Hence, this picture may indicate that the observed better electrical conductivity of the BC/SnO_2 anode over that of BC in LIBs and NIBs mainly results from the formation of Sn-based alloys under working conditions. To explain these complex phenomena and elucidate the role of individual components in the redox processes, further theoretical studies are needed.

4 Conclusion

The BC/SnO_2 composite anode material was synthesized *via* a facile thermochemical process involving hydrothermal carbonization with H_3PO_4 followed by pyrolysis, which provoked an extraordinary change in their porous structure. The XPS indicated a successful incorporation of Sn atoms (8.9 wt%, atomic percentage). The BC/SnO_2 yielded a macroporous structure rich in defects that are helpful for filling more Sn atoms into the biochar and enhancing the insertion and extraction of metal ions (Li^+, Na^+). When tested as anodes in LIBs and NIBs, the BC/SnO_2 anode exhibited a better performance. For LIBs, the BC/SnO_2 anode delivered a specific capacity of 319 mA h g^{-1} while BC delivered 93.2 mA h g^{-1} at 1C (120 cycles). Moreover, when BC/SnO_2 was subjected to a cycling performance at 0.1C, it exhibited a capacity of 453 mA h g^{-1} at the end of 120 cycles. When both samples were tested in NIBs, BC/SnO_2 exhibited higher capacity during all cycles than the BC anode, delivering a 233 mA h g^{-1} capacity at the end of 120 cycles. In comparison, BC delivered a capacity of 165 mA h g^{-1} at 100 mA g^{-1}. Our novel macroporous BC/SnO_2 synthesis strategy offers a promising and facile way of designing suitable, stable carbon–metal composite anodes for enhanced LIB and NIB performances. Based on the semiempirical GFN1-xTB calculations the tin oxide does not put its electronic states close to the Fermi level of the mixed system, hence the observed better electrical conductivity over that of BC should originate from the formation of Sn-based alloys under working conditions. This research may offer new and suitable research directions for producing biomass-based carbon–metal macroporous anode materials for efficient alkali-metal-ion battery applications.

Data availability

The data that support the findings of this study are available from the corresponding author upon reasonable request.

Conflicts of interest

The authors of this paper claim no conflicts of interest.

Acknowledgements

Dr Glaydson dos Simoes Reis gratefully acknowledges financial support from the Research Council of Finland (Academy Research Fellows 2024, Project: Bio-Adsorb&Energy, grant no. 361583). This work was supported by the EU/Interreg Aurora (Project GreenBattery, grant no 20357574). The authors also acknowledge Business Finland for research funding 2024-2027, the University of Oulu (BATCircle3.0, No. 2196/31/2024). Dr Grimm acknowledges financial support from the Swedish Research Council Formas (grant No. 2021–00877) and Kempestiftelserna (grant no. JCSMK23-0145). FG and CMS thank MCIN/AEI/10.13039/501100011033 for funding the project PID2022-139039OB-C21. We gratefully acknowledge the Polish high-performance computing infrastructure PLGrid (HPC Center: ACK Cyfronet AGH) for providing computer facilities and support within computational grant no. PLG/2020/013980.

References

1 Y. L. Zhukovskiy, D. E. Batueva, A. D. Buldysko, B. Gil and V. V. Starshaia, Fossil Energy in the Framework of Sustainable Development: Analysis of Prospects and Development of Forecast Scenarios, *Energies*, 2021, **14**(17), 5268.
2 M. Li, J. Lu, Z. Chen and K. Amine, 30 Years of Lithium-Ion Batteries, *Adv. Mater.*, 2018, **30**, 1800561.
3 P. Molaiyan, B. Boz, G. S. dos Reis, R. Sliz, S. Wang, M. Borsari, U. Lassi and A. Paolella, Paving the path toward silicon as anode material for future solid-state batteries, *eTransportation*, 2025, **23**, 100391.
4 M. Abdollahifar, P. Molaiyan, U. Lassi, N. L. Wu and A. Kwade, Multifunctional behaviour of graphite in lithium–sulfur batteries, *Renewable Sustainable Energy Rev.*, 2022, **169**, 112948.
5 H. Ahmed, S. Dos R. Glaydson, P. Molaiyan, A. Lähde and U. Lassi, Silicon/carbon composite anode materials for

lithium-ion batteries: Materials design and synthesis, current state, progress, and future perspectives, *Prog. Energy*, 2025, **7**, 022003.

6 P. Molaiyan, G. S. Dos Reis, D. Karuppiah, C. M. Subramaniyam, F. García-Alvarado and U. Lassi, Recent Progress in Biomass-Derived Carbon Materials for Li-Ion and Na-Ion Batteries—A Review, *Batteries*, 2023, **9**, 116.

7 K. Nobuhara, H. Nakayama, M. Nose, S. Nakanishi and H. Iba, First-principles study of alkali metal-graphite intercalation compounds, *J. Power Sources*, 2013, **243**, 585–587.

8 W. Zhang, J. Lu and Z. Guo, Challenges and future perspectives on sodium and potassium ion batteries for grid-scale energy storage, *Mater. Today*, 2021, **50**, 400–417.

9 F. Xie, Z. Xu, Z. Guo and M.-M. Titirici, Hard carbons for sodium-ion batteries and beyond, *Prog. Energy*, 2020, **2**, 42002.

10 P. Chaudhary, S. Bansal, B. B. Sharma, S. Saini and A. Joshi, Waste biomass-derived activated carbons for various energy storage device applications: A review, *J. Energy Storage*, 2024, **78**, 109996.

11 G. S. dos Reis, D. Bergna, A. Grimm, E. C. Lima, T. Hu, M. Naushad and U. Lassi, Preparation of highly porous nitrogen-doped biochar derived from birch tree wastes with superior dye removal performance, *Colloids Surf., A*, 2023, **669**, 131493.

12 G. Simões dos Reis, C. Mayandi Subramaniyam, A. D. Cárdenas, S. H. Larsson, M. Thyrel, U. Lassi and F. García-Alvarado, Facile Synthesis of Sustainable Activated Biochars with Different Pore Structures as Efficient Additive-Carbon-Free Anodes for Lithium- and Sodium-Ion Batteries, *ACS Omega*, 2022, **7**, 42570–42581.

13 A. Daulay, Andriayani, Marpongahtun, S. Gea and Tamrin, Scalable synthesis of porous silicon nanoparticles from rice husk with the addition of KBr as a scavenger agent during reduction by the magnesiothermic method as anode lithium-ion batteries with sodium alginate as the binder, *S. Afr. J. Chem. Eng.*, 2022, **41**, 203–210.

14 J. Zhang, D. Zhang, K. Li, Y. Tian, Y. Wang and T. Sun, N, O and S co-doped hierarchical porous carbon derived from a series of samara for lithium and sodium storage: Insights into surface capacitance and inner diffusion, *J. Colloid Interface Sci.*, 2021, **598**, 250–259.

15 T. K. Pham, J. H. Shin, N. C. Karima, Y. S. Jun, S.-K. Jeong, N. Cho, Y.-W. Lee, Y. Cho, S. N. Lim and W. Ahn, Application of recycled Si from industrial waste towards Si/rGO composite material for long lifetime lithium-ion battery, *J. Power Sources*, 2021, **506**, 230244.

16 V. Ahuja, B. Senthilkumar and P. Senguttuvan, Ultra-stable Sb/hard carbon composite anodes with synergistic alkali-ion storage performances, *Mater. Res. Bull.*, 2021, **144**, 111491.

17 Z. Chen, D. Yin and M. Zhang, Sandwich-like MoS2@SnO2@C with High Capacity and Stability for Sodium/Potassium Ion Batteries, *Small*, 2018, **14**, 1703818.

18 M. Lao, Y. Zhang, W. Luo, Q. Yan, W. Sun and S. X. Dou, Alloy-Based Anode Materials toward Advanced Sodium-Ion Batteries, *Adv. Mater.*, 2017, **29**, 1700622.

19 C. Zhao, C. Yu, M. Zhang, H. Huang, S. Li, X. Han, Z. Liu, J. Yang, W. Xiao, J. Liang, X. Sun and J. Qiu, Ultrafine MoO2-Carbon Microstructures Enable Ultralong-Life Power-Type Sodium Ion Storage by Enhanced Pseudocapacitance, *Adv. Energy Mater.*, 2017, **7**, 1602880.

20 Y. Xu, Y. Zhu, Y. Liu and C. Wang, Electrochemical Performance of Porous Carbon/Tin Composite Anodes for Sodium-Ion and Lithium-Ion Batteries, *Adv. Energy Mater.*, 2013, **3**, 128–133.

21 Y. Liu, X.-Y. Yu, Y. Fang, X. Zhu, J. Bao, X. Zhou and X. W. (David) Lou, Confining SnS2 Ultrathin Nanosheets in Hollow Carbon Nanostructures for Efficient Capacitive Sodium Storage, *Joule*, 2018, **2**, 725–735.

22 B. Huang, J. Yang and X. Zhou, Hierarchical SnO2 with double carbon coating composites as anode materials for lithium ion batteries, *J. Solid State Electrochem.*, 2014, **18**, 2443–2449.

23 R. Li, L. Qing, W. Emori, W. Su, W. Zhao, J. Chen, G. T. Yu and J. H. Lin, Ultrafine SnO_2 Nanoparticles Decorated on N-Doped Highly Structurally Connected Carbon Nanospheres as Anode Materials for High-Performance Sodium-Ion Batteries, *Energy Fuels*, 2022, **36**, 4957–4966.

24 Y. Li, X. Zhang, R. Yang, G. Li and C. Hu, The role of H_3PO_4 in the preparation of activated carbon from NaOH-treated rice husk residue, *RSC Adv.*, 2015, **5**, 32626–32636.

25 I. Neme, G. Gonfa and C. Masi, Activated carbon from biomass precursors using phosphoric acid: A review, *Heliyon*, 2022, **8**, e11940.

26 G. S. dos Reis, J. Thivet, E. Laisné, V. Srivastava, A. Grimm, E. C. Lima, D. Bergna, T. Hu, M. Naushad and U. Lassi, Synthesis of novel mesoporous selenium-doped biochar with high-performance sodium diclofenac and reactive orange 16 dye removals, *Chem. Eng. Sci.*, 2023, **281**, 119129.

27 S. Grimme, C. Bannwarth and P. Shushkov, A Robust and Accurate Tight-Binding Quantum Chemical Method for Structures, Vibrational Frequencies, and Noncovalent Interactions of Large Molecular Systems Parametrized for All spd-Block Elements (Z = 1–86), *J. Chem. Theory Comput.*, 2017, **13**, 1989–2009.

28 B. Hourahine, B. Aradi, V. Blum, F. Bonafé, A. Buccheri, C. Camacho, C. Cevallos, M. Y. Deshaye, T. Dumitrică, A. Dominguez, S. Ehlert, M. Elstner, T. van der Heide, J. Hermann, S. Irle, J. J. Kranz, C. Köhler, T. Kowalczyk, T. Kubař, I. S. Lee, V. Lutsker, R. J. Maurer, S. K. Min, I. Mitchell, C. Negre, T. A. Niehaus, A. M. N. Niklasson, A. J. Page, A. Pecchia, G. Penazzi, M. P. Persson, J. Řezáč, C. G. Sánchez, M. Sternberg, M. Stöhr, F. Stuckenberg, A. Tkatchenko, V. W.-z Yu and T. Frauenheim, DFTB+, a software package for efficient approximate density functional theory based atomistic simulations, *J. Chem. Phys.*, 2020, **152**, 124101.

29 M. Elstner, D. Porezag, G. Jungnickel, J. Elsner, M. Haugk, T. Frauenheim, S. Suhai and G. Seifert, Self-consistent-charge density-functional tight-binding method for simulations of complex materials properties, *Phys. Rev. B: Condens. Matter Mater. Phys.*, 1998, **58**, 7260–7268.

30 S. Grimme, J. Antony, S. Ehrlich and H. Krieg, A consistent and accurate ab initio parametrization of density functional dispersion correction (DFT-D) for the 94 elements H-Pu, *J. Chem. Phys.*, 2010, **132**, 154104.
31 H. J. Monkhorst and J. D. Pack, Special points for Brillouin-zone integrations, *Phys. Rev. B*, 1976, **13**, 5188–5192.
32 V. L. Deringer, M. A. Caro, R. Jana, A. Aarva, S. R. Elliott, T. Laurila, G. Csányi and L. Pastewka, Computational Surface Chemistry of Tetrahedral Amorphous Carbon by Combining Machine Learning and Density Functional Theory, *Chem. Mater.*, 2018, **30**, 7438–7445.
33 G. J. Martyna, M. E. Tuckerman, D. J. Tobias and M. L. Klein, Explicit reversible integrators for extended systems dynamics, *Mol. Phys.*, 1996, **87**, 1117–1157.
34 S. Kirkpatrick, C. D. Gelatt and M. P. Vecchi, Optimization by Simulated Annealing, *Science*, 1983, **220**, 671–680.
35 M. Thommes, K. Kaneko, A. V. Neimark, J. P. Olivier, F. Rodriguez-Reinoso, J. Rouquerol and K. S. W. Sing, Physisorption of gases, with special reference to the evaluation of surface area and pore size distribution (IUPAC Technical Report), *Pure Appl. Chem.*, 2015, **87**, 1051–1069.
36 J. H. Um, M. Choi, H. Park, Y.-H. Cho, D. C. Dunand, H. Choe and Y.-E. Sung, 3D macroporous electrode and high-performance in lithium-ion batteries using SnO_2 coated on Cu foam, *Sci. Rep.*, 2016, **6**, 18626.
37 J. Wang, J. Wang, X. Guo and H. Yang, Construction of Macroporous Co_2SnO_4 with Hollow Skeletons as Anodes for Lithium-Ion Batteries, *Gels*, 2022, **8**, 257.
38 L. Zeng, A. R. Thiruppathi, J. van der Zalm, X. Li and A. Chen, Biomass-derived amorphous carbon with localized active graphite defects for effective electrocatalytic N_2 reduction, *Appl. Surf. Sci.*, 2022, **575**, 151630.
39 M. González-Hourcade, G. Simões dos Reis, A. Grimm, V. M. Dinh, E. C. Lima, S. H. Larsson and F. G. Gentili, Microalgae biomass as a sustainable precursor to produce nitrogen-doped biochar for efficient removal of emerging pollutants from aqueous media, *J. Cleaner Prod.*, 2022, **348**, 131280.
40 M. Pawlyta, J.-N. Rouzaud and S. Duber, Raman microspectroscopy characterization of carbon blacks: Spectral analysis and structural information, *Carbon*, 2015, **84**, 479–490.
41 G. Xu, L. Zhang, C. Guo, L. Gu, X. Wang, P. Han, K. Zhang, C. Zhang and G. Cui, Manganese monoxide/titanium nitride composite as high performance anode material for rechargeable Li-ion batteries, *Electrochim. Acta*, 2012, **85**, 345–351.
42 X. Ren, F. Zhang, T. Fang, Q. Zhang, S. Zhong and W. Yao, Tin-carbon composite submicron spheres constructed by molten salt synthesis and their high lithium storage performance, *Mater. Today Commun.*, 2024, **38**, 108562.
43 S. S. Badadhe, P. Yadav, S. Suryawanshi and M. A. More, Facile synthesis of nanocomposites of CNF-Sn and C-Sn microspheres: Prospective field emitter, *J. Alloys Compd.*, 2022, **907**, 164318.
44 B. Peng, Y. Xu, K. Liu, X. Wang and F. M. Mulder, High-Performance and Low-Cost Sodium-Ion Anode Based on a Facile Black Phosphorus−Carbon Nanocomposite, *ChemElectroChem*, 2017, **4**, 2140–2144.
45 G. Moreno-Fernández, M. Granados-Moreno, J. L. Gómez-Urbano and D. Carriazo, Phosphorus-Functionalized Graphene for Lithium-Ion Capacitors with Improved Power and Cyclability, *Batteries Supercaps*, 2021, **4**, 469–478.
46 E. H. Ramírez-Soria, S. García-Dalí, J. M. Munuera, D. F. Carrasco, S. Villar-Rodil, J. M. D. Tascón, J. I. Paredes and J. Bonilla-Cruz, A Simple and Expeditious Route to Phosphate-Functionalized, Water-Processable Graphene for Capacitive Energy Storage, *ACS Appl. Mater. Interfaces*, 2021, **13**, 54860–54873.
47 S. T. Mahmud, R. Mia, S. Mahmud, S. Sha, R. Zhang, Z. Deng, M. Yanilmaz, L. Luo and J. Zhu, Recent Developments of Tin (II) Sulfide/Carbon Composites for Achieving High-Performance Lithium Ion Batteries: A Critical Review, *Nanomaterials*, 2022, **12**, 1246.
48 B. K. Chakrabarti, G. Bree, A. Dao, G. Remy, M. Ouyang, K. B. Dönmez, B. Wu, M. Williams, N. P. Brandon, C. George and C. T. J. Low, Lightweight Carbon–Metal-Based Fabric Anode for Lithium-Ion Batteries, *ACS Appl. Mater. Interfaces*, 2024, **16**, 21885–21894.
49 M. Ye, J. Ye, Z. Zhang, Z. Feng, D. Xiong and M. He, Construction of porous-carbon supported core-shell SnO_2@$BaTiO_3$ nanosphere heterostructures as anode for high-performance sodium-ion battery, *J. Power Sources*, 2025, **630**, 236160.
50 N. R. Srinivasan, S. Al-Rubaye and C. M. Subramaniyam, Structural properties and electrochemical performances of mesoporous carbon towards enhanced lithium-ion storage, *Chem. Inorg. Mater.*, 2024, **2**, 100032.
51 L. Sun, X. Wang, R. A. Susantyoko and Q. Zhang, High performance binder-free Sn coated carbon nanotube array anode, *Carbon*, 2015, **82**, 282–287.
52 M. V. Reddy, L. Yu Tse, W. K. Z. Bruce and B. V. R. Chowdari, Low temperature molten salt preparation of nano-SnO_2 as anode for lithium-ion batteries, *Mater. Lett.*, 2015, **138**, 231–234.
53 P. Nithyadharseni, K. P. Abhilash, S. Petnikota, M. R. Anilkumar, R. Jose, K. I. Ozoemena, R. Vijayaraghavan, P. Kulkarni, G. Balakrishna, B. V. R. Chowdari, S. Adams and M. V. Reddy, Synthesis and Lithium Storage Properties of Zn, Co and Mg doped SnO_2 Nano Materials, *Electrochim. Acta*, 2017, **247**, 358–370.
54 C. Liang, J. Guo, L. Yue, M. Wang, J. Liang, X. Wang, Y. Li and K. Yu, MOF-SnO_2 nanoparticles composited with biomass-derived carbon used as high-performance anodes for lithium-ion batteries, *Diamond Relat. Mater.*, 2023, **140**, 110488.
55 Q. Tian, Z. Zhang, L. Yang and S. Hirano, Encapsulation of SnO_2/Sn Nanoparticles into Mesoporous Carbon Nanowires and its Excellent Lithium Storage Properties, *Part. Part. Syst. Charact.*, 2015, **32**, 381–388.
56 Y. Chen, C. Han and J. Zhu, Self-assembly design of novel tin/lignite–derived graphene–like porous carbon composite for lithium–ion battery, *Diamond Relat. Mater.*, 2023, **131**, 109610.

57 S. Petnikota, G. Simões Dos Reis, F. A. Kayakool, V. S. S. S. Vadali, J. Välikangas, U. Lassi and M. Thyrel, Microwave Exfoliated Few-Layered Graphene Cathode for Aluminum Batteries, *ACS Appl. Energy Mater.*, 2024, **7**, 6862–6872.

58 S. Petnikota, S. K. Marka, A. Banerjee, M. V. Reddy, V. V. S. S. Srikanth and B. V. R. Chowdari, Graphenothermal reduction synthesis of 'exfoliated graphene oxide/iron (II) oxide' composite for anode application in lithium ion batteries, *J. Power Sources*, 2015, **293**, 253–263.

59 S. Petnikota, J. J. Toh, J. Y. Li, R. Chua and M. Srinivasan, Citric Acid Assisted Solid State Synthesis of V_2O_3, V_2O_3/C and V_2O_3/Graphene Composites for Li-ion Battery Anode Applications, *ChemElectroChem*, 2019, **6**, 493–503.

60 H. Maseed, S. Petnikota, V. V. S. S. Srikanth, N. K. Rotte, M. Srinivasan, F. Bonaccorso, V. Pellegrini and M. V. Reddy, A new insight into Li-staging, in-situ electrochemical exfoliation, and superior Li storage characteristics of highly crystalline few-layered graphene, *J. Energy Storage*, 2021, **41**, 102908.

61 N. Sun, Z. Guan, Y. Liu, Y. Cao, Q. Zhu, H. Liu, Z. Wang, P. Zhang and B. Xu, Extended ''Adsorption–Insertion'' Model: A New Insight into the Sodium Storage Mechanism of Hard Carbons, *Adv. Energy Mater.*, 2019, **9**, 1901351.

62 F. Jiang, F. Luo, Q. Fan, P. Guo, Y. Liao, M. Chen, C. Liu, J. Chen, D. Wang and Z. Zheng, A composite material consisting of tin nanospheres anchored on and embedded in carbon nanofibers for outstanding sodium-ion storage, *J. Electroanal. Chem.*, 2024, **959**, 118186.

63 W. He, K. Chen, R. Pathak, M. Hummel, K. M. Reza, N. Ghimire, J. Pokharel, S. Lu, Z. Gu, Q. Qiao and Y. Zhou, High-mass-loading Sn-based anode boosted by pseudocapacitance for long-life sodium-ion batteries, *Chem. Eng. J.*, 2021, **414**, 128638.

64 M. Sha, H. Zhang, Y. Nie, K. Nie, X. Lv, N. Sun, X. Xie, Y. Ma and X. Sun, Sn nanoparticles@nitrogen-doped carbon nanofiber composites as high-performance anodes for sodium-ion batteries, *J. Mater. Chem. A*, 2017, **5**, 6277–6283.

65 M. Han, C. Zhu, Q. Zhao, C. Chen, Z. Tao, W. Xie, F. Cheng and J. Chen, In Situ Atomic Force Microscopic Studies of Single Tin Nanoparticle: Sodiation and Desodiation in Liquid Electrolyte, *ACS Appl. Mater. Interfaces*, 2017, **9**, 28620–28626.

